

Fabrication of low-tortuosity thick electrodes with low material loss by temporally shaped ultraviolet femtosecond laser

Received: 27 October 2024

Accepted: 5 December 2025

Published online: 23 December 2025

 Check for updates

Junrui Wu^{1,2}, Huixin Guo³, Ruoxi Wang¹, Lan Jiang^{1,2}, Xin Li^{1,2} ✉, Jiang Zhang¹, Richen Jia¹, Mengyao Tian¹, Yu Liu¹, Xiaofeng Wang^{1,4}, Ran Zhao⁵, Xiangbiao Liao³ & Qian Cheng^{1,2} ✉

Conventional battery electrodes exhibit high tortuosity, which severely impedes ion transport. This limitation restricts electrode thickness, decreases power density, and shortens battery lifetime. Fabricating through-holes can reduce tortuosity, but existing methods are generally complex with poor space utilization. Here, an array of high-density through-holes are fabricated by temporally shaped ultraviolet femtosecond laser. Using this technique, we achieve a 47:1 aspect ratio (6 μm in diameter), ensuring low material loss (<1%) for 280 μm -thick LiFePO_4 (LFP) electrodes. The through-hole array reduces tortuosity of LFP thick electrodes by 19.1% (30 mg cm^{-2}), 19.0% (40 mg cm^{-2}), and 20.2% (60 mg cm^{-2}), improving the specific energy density of batteries by 9.39%, 12.27%, 17.39% at 1 C, 1.5 C, and 2 C, respectively. It also boosts LFP power density by 100%–200% and doubles the cycling lifetime. This work demonstrates an effective approach for fabricating low-tortuosity thick electrodes, enhancing comprehensive performance of batteries.

Lithium-ion batteries (LIBs) are widely used in portable electronics, electric vehicles, and large-scale energy storage systems due to their high energy density, high operating voltage, and long cycling lifetime^{1–4}. However, increased demands for higher energy density, power density, and longer cycling lifetime have set benchmarks for LIBs^{5–8}. While developing emerging battery materials with enhanced performance is challenging, designing battery electrode structures that facilitate electron/ion transport and increase the ratio of active material presents a viable approach to improving battery performance. For instance, the active material thickness has a practical limit (Fig. 1a), typically around 50–70 μm ⁹. This limitation arises from the highly compacted structure of electrodes due to the calendaring process (Fig. 1b), which often results in high tortuosity. High

tortuosity not only hinders electrolyte infiltration but also leads to a convoluted and lengthy path for ion transport, lowering rates and capacity^{9–11}. In thick electrodes, ion transport has become a major bottleneck for improving battery performance. Therefore, it is crucial to manufacture low-tortuosity electrodes.

Low-tortuosity electrodes, such as electrodes with through-holes (Fig. 1c), can enhance the power density, energy density, and cycling lifetime. Through-holes generally refer to holes that extend all the way through the current collector. For power density, through-holes provide direct pathways for ion diffusion, reducing internal resistance and thus enabling higher rates^{12–14}. For energy density, the decreased internal resistance and enhanced ion transport allow for the use of thicker electrodes, increasing the ratio of active material and thereby

¹Laser Micro/Nano-Fabrication Laboratory, School of Mechanical Engineering, Beijing Institute of Technology, Beijing, PR China. ²Complex Microstructure Processing Technology (National) Innovation Center, Beijing, PR China. ³Advance Research Institute of Multidisciplinary Sciences, Beijing Institute of Technology, Beijing, PR China. ⁴Shenzhen Thinkpart Materials Technology Co. Ltd, Shenzhen, PR China. ⁵Beijing Key Laboratory of Environmental Science and Engineering, Beijing, PR China. ✉e-mail: lixin02@bit.edu.cn; qiancheng@bit.edu.cn

enhancing energy density^{15,16}. Additionally, through-holes are less likely to become blocked compared to microstructures in traditional electrodes, resulting in more stable cycling performance^{17,18}.

Given these advantages, considerable efforts have been made to fabricate low-tortuosity electrodes, with template methods being the most widely employed techniques. These include magnetic alignment¹⁹, phase inversion method²⁰, freeze-casting method^{21,22} and a modified ice-templating process²³ (Supplementary Table 1). Despite these advancements, challenges persist, including complex fabrication processes, incompatibility with existing manufacturing workflows, and, particularly, unsuitability for calendaring. Calendaring is crucial as it reduces electrode porosity and improves internal electrical contact^{24,25}. However, these template methods are incompatible with calendaring, as the process can partially or completely collapse the aligned-pore structures. As a result, the pore-engineered electrodes typically exhibit excessively high porosities (40–70%, Supplementary Table 1). This compromises the potential advantages of higher energy density that can be achieved with thicker electrodes¹³. For a battery using LFP as positive electrode and lithium metal as negative electrode, an increase in LFP layer thickness from 60 μm to 260 μm results in a 46.0% increase in specific energy density. However, the introduction of low-tortuosity aligned pores usually increases the porosity by more than 20%, resulting in a 17.1% reduction in specific energy density. This weakens the specific energy density gains achieved by thick electrodes (Fig. 1d). Similar patterns are observed in volumetric energy density, where the issue is even more pronounced due to the high porosity resulting in the waste of battery space (Supplementary Fig. 1).

Laser can manufacture micro-holes by focusing it on the sample surface, thereby increasing the temperature at the focused spot through energy accumulation^{26–28}. This causes the material to undergo photothermal (melt, vaporize, and ionize) or photochemical reactions, thereby forming holes^{29–31}. It provides advantages such as non-contact and flexible machining, low cost, fast processing speed, etc. Moreover, as a post-treatment method, it is compatible with existing manufacturing workflows, including the calendaring process, making it a highly effective solution. Emani et al. used ultrafast laser to introduce structured pore networks and reduce tortuosity, enhancing capacity and rate performance³². Another effort applied laser patterning to develop 3D channel architectures in thick graphite negative electrodes³³ and silicon/graphite composite negative electrodes³⁴, improving capacity and cycling performance under fast charging conditions. Although these developments demonstrate the application of laser patterning techniques in producing low-tortuosity electrodes, the challenge of low space utilization still exists, with all these works reporting high material loss (10–20%, Supplementary Table 1) and large hole spacing during laser processing. Therefore, it is crucial to develop methods that can create dense micropore arrays in thick electrodes with low material loss, aiming to significantly reduce tortuosity while maintaining high space utilization.

In this report, we present a femtosecond laser percussion drilling method with frequency/time domain shaping techniques to fabricate high-density micro-through-hole arrays in any battery electrode. The resulting holes feature a radius of approximately 6 μm in electrodes with thicknesses up to 280 μm , achieving a maximum aspect ratio of 47 and low material loss of <1%. The through-hole array reduces the tortuosity of thick electrodes by ~20%, significantly enhancing rate performance for LFP electrodes and NMC electrodes, with the power density increasing by 100–400% (Fig. 1e). The thickest laser-structured LFP electrode with an areal mass loading of 60 mg cm^{-2} exhibits capacities of 139.4, 125.63 and 84.86 mAh g^{-1} at 0.5 C, 1 C, and 1.5 C, respectively. In contrast, an identical LFP electrode without laser structuring showed capacities of 108.07, 23.63 and 8.48 mAh g^{-1} at 0.5 C, 1 C, and 1.5 C, respectively. Similar rate performance improvements were also observed for the thick NMC electrodes. This allows

LFP for increase in mass loading from 14 mg cm^{-2} to 30–60 mg cm^{-2} , corresponding to a specific energy increase of 9.39% to 17.39%. Furthermore, the cycling stability is markedly enhanced, with the cycling lifetime doubled. This study highlights the effectiveness of our method in developing low-tortuosity electrodes with low mass loss, offering a practical method to enhance energy density, power density, and lifetime of batteries.

Results

Fabrication and characterization of through-holes with small diameters and high-aspect ratios

To achieve low-tortuosity thick electrodes with low material loss, it is essential to fabricate high-quality through-holes with small diameters and high aspect ratios. However, this remains challenging due to the inherently porous and fragile electrode structure. During the laser drilling process, the electrode is easily affected by thermal or stress damage, resulting in excessive material loss. To this end, a Ti:Sapphire laser with 800 nm wavelength and 35 fs pulse was selected because its ultrashort pulses and high peak intensity allow electrons to absorb photon energy before the lattice temperature rises, resulting in significantly smaller thermal effects and thus a higher aspect ratio. The opacity of electrode materials makes it challenging to fabricate through-holes with small diameters and high aspect ratios, as conventional spatial modulation methods, such as Bessel beam shaping, cannot be used. Therefore, a multi-pulse percussion drilling method was adopted for micro-hole machining in electrodes, in which the holes are fabricated by repeated impacts from hundreds of laser pulses (Fig. 1f). The aspect ratio of a hole is theoretically limited by the quality of the focused beam³⁵, including the size of the processing laser spot, the depth of focus, and the laser power. The diameters of the holes are affected by the focal laser spot size ($2w_0$) and focal depth ($2z_0$), which is given by ref. 36:

$$2w_0 = 2\lambda/(\pi NA) \quad (1)$$

$$2z_0 = kw_0^2 \quad (2)$$

where $2w_0$ is the diameter of the focused laser spot, $2z_0$ is the focal depth of the focused laser spot, λ is the wavelength of the laser light, and NA is the numerical aperture of the lens. As indicated by Eq. 1, achieving a smaller hole diameter requires reducing the laser beam size, which can be accomplished by decreasing the wavelength and increasing the NA of the lens. However, it is not feasible to continuously increase the NA because the focal depth decreases as the NA of the objective lens increases (Eq. 2). If the NA is too high, through-holes cannot be fabricated due to limited focal depth (Supplementary Table 2). Therefore, it is necessary to balance the beam size and focal depth by carefully adjusting the NA and laser wavelength.

Objective lenses with different NA values (0.15–0.8) and femtosecond lasers with different wavelengths (800 nm and 400 nm) were used to perform multi-pulse percussion drilling experiments on 40 mg cm^{-2} LFP thick electrodes (190 μm). Scanning Electron Microscopy (SEM) and optical microscopy were used to examine both surfaces of the electrode to determine if through-holes were fabricated. When using lower NAs such as 0.15, 0.3, it is challenging to focus the femtosecond laser on the electrode to form through-holes (Supplementary Fig. 2a–b). This is because both the spot diameter and the focal depth are large, resulting in low laser energy density (Supplementary Fig. 3a–b). When the NA increases from 0.4 to 0.45 and 0.5 (Fig. 2a–c and Supplementary Fig. 2c–e), it becomes possible to fabricate through-holes, with apertures narrowing from 20 μm to 15 μm , and then to 10 μm , respectively. When the NA is further increased to 0.8, through-holes cannot be fabricated due to the relatively short focal depth (Supplementary Fig. 2f and Supplementary Fig. 3c).

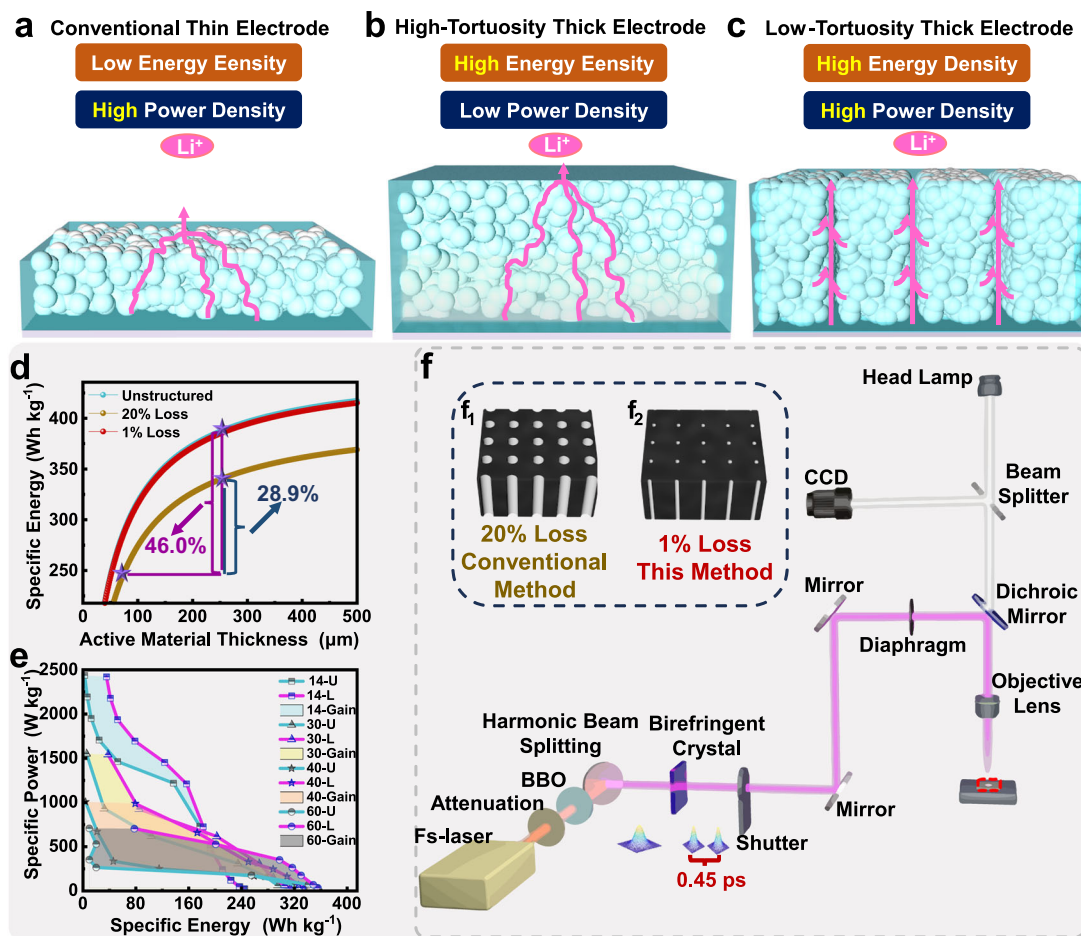


Fig. 1 | Challenges and solutions in manufacturing low-tortuosity thick electrodes. The schematics of **a** conventional thin electrode, **b** high-tortuosity thick electrode, and **c** low-tortuosity thick electrodes with through-holes. **d** The relationship between specific energy density and active material thickness in Li||LFP batteries. Calculations can be found in Supplementary Note 1. **e** The Ragone plot of

laser-structured LiFePO₄ (LFP) electrodes and unstructured LFP electrodes. The numbers refer to the areal mass loading, while 'U' and 'L' stand for unstructured electrode and laser-structured electrode, and 'Gain' refers to the increase in specific power and specific energy at the same areal mass loading. **f** The schematic diagram of the laser processing system with frequency/time domain shaping techniques.

Furthermore, a BBO crystal was employed for frequency domain shaping to double the laser frequency and convert the wavelength from 800 nm to 400 nm, successfully reducing the through-hole diameter from 10 μm to 6 μm (Fig. 2d). The relationship between pore size and NA and the mechanisms are summarized in Fig. 2e, f, respectively.

We next tried to optimize hole distribution to enhance electrolyte penetration and facilitate ion diffusion, with the prerequisite of low material loss (<1%). As discussed earlier, 6 μm is the smallest achievable hole diameter using our method. To realize a material loss of below 1%, the hole spacing can be determined to be 60 μm, with the longest ion diffusion length of 42 μm in electrode microstructure (Supplementary Fig. 4). This sample is labeled as 6–60 μm, using a 'hole diameter-hole spacing' format. We further fabricated 6–60 μm, 10–120 μm, 20–240 μm, and 30–360 μm structures on 190 μm thick LFP electrodes, all with the same material loss (<1%). These LFP electrodes were assembled into half-cells, and their electrochemical performances were compared. The results showed that the 6–60 μm configuration performed better than the 10–120 μm setup, which in turn was more effective than the 20–240 μm electrode, and significantly exceeded the 30–360 μm electrode and the unstructured electrode (Fig. 2g). This pattern can be attributed to the shorter ion diffusion path within the electrode microstructure, which reduces internal resistance and improves rate performance.

To further validate the enhancement of electrode-level ion diffusion enabled by laser-structured through-holes, simulations of the

discharging process were performed using COMSOL Multiphysics. Four electrode structures were simulated, representing unstructured, 6–60 μm, 10–120 μm, and 20–240 μm hole configurations (Fig. 3a). The results also demonstrated that electrodes with the 6–60 μm hole configuration achieve higher discharge capacities at elevated C-rates compared to both larger but diluted pore structured configurations and the unstructured electrode (Fig. 3b). The enhanced rate performance of the 6–60 μm structured electrode is attributed to better ionic transport. Fig. 3c–e and Supplementary Fig. 5 illustrate the salt concentration evolution over time during 1C discharge for both structured (6–60 μm) and unstructured electrodes. In unstructured electrodes, a steep concentration gradient starts to develop during the reaction, eventually leading to localized lithium-ion depletion. By the end of discharge (2250 s), the electrolyte salt concentration at the bottom of the electrode ($Z=0-40$ μm) had reached zero, halting the electrochemical reaction due to the lack of available lithium ions (Fig. 3f). This severe transport limitation results from the high tortuosity of unstructured LFP. In contrast, the laser-structured electrode maintains a more uniform electrolyte concentration profile throughout the discharge process. The through-holes enhance ionic transport pathways, avoid localized depletion, and sustain continuous reaction activity. Even at the end of discharging period (2250–3194 s), the salt concentration at the bottom of the electrode ($Z=0-40$ μm) remains significantly higher, ensuring full capacity utilization at 1C (Fig. 3g). These findings confirm that optimizing ionic transport and reaction

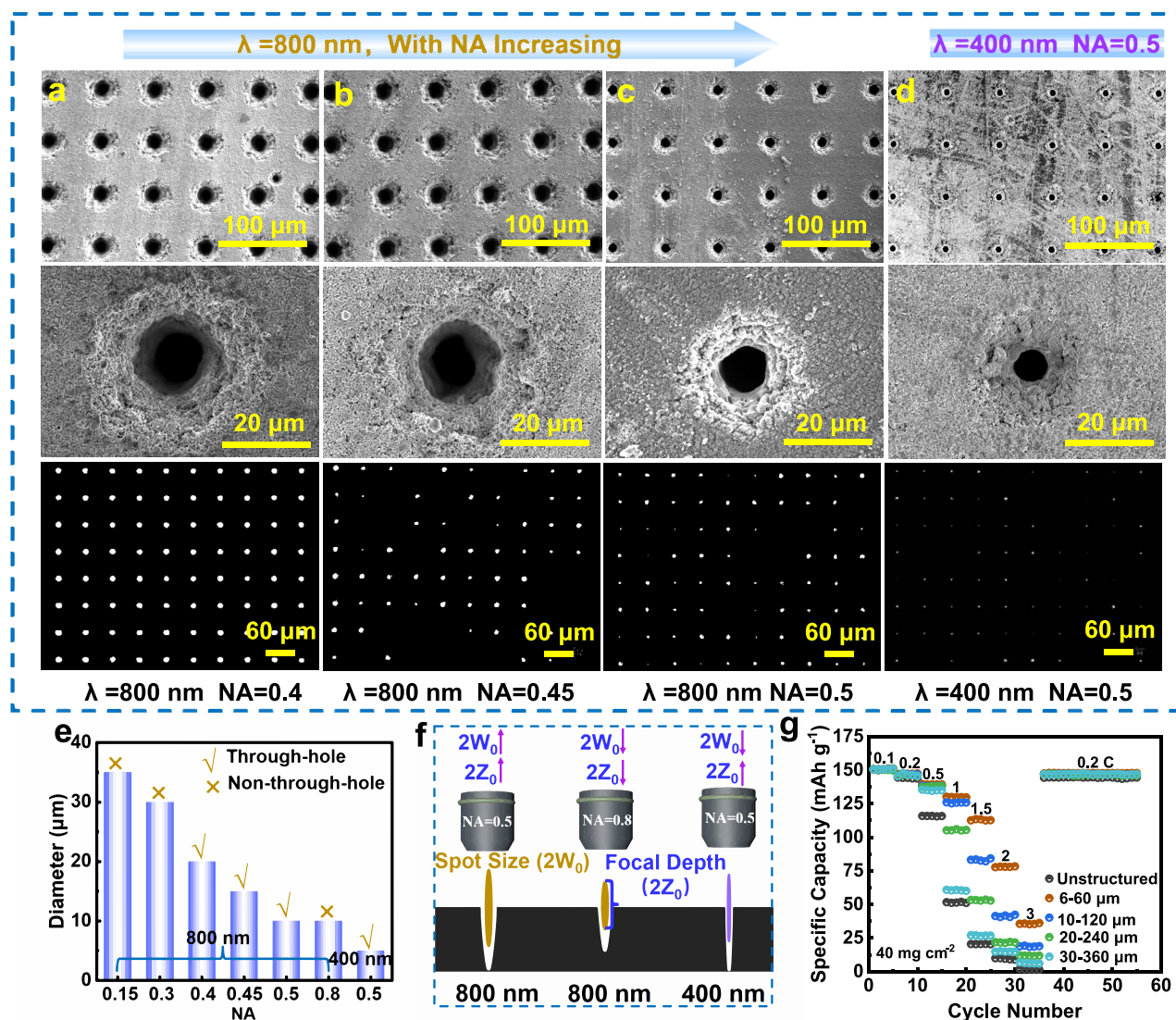


Fig. 2 | The method to minimize material loss of LFP electrodes during laser percussion drilling. a–d SEM and backlight microscope images showing micro-hole arrays created by femtosecond laser percussion drilling with different Numerical Aperture (NA = 0.4, 0.45, 0.5) objective lenses and different wavelengths (800 nm, 400 nm). e The relationship between aperture size across different NAs

and wavelengths. f The effects of objective lens NA and laser wavelength on the diameter and aspect ratio of laser-drilled holes. g Influence of hole size/distribution on rate performance, including configurations of 6–60 μm, 10–120 μm, 20–240 μm, 30–360 μm.

uniformity requires more small holes with dense distribution. Moving forward, all laser-structured low-tortuosity thick electrodes were designed based on the 6–60 μm configuration, which proved to be the most effective for enhancing ion transport and rate capability.

With 6–60 μm being the optimal structure, we further examined its impact across electrodes of different thicknesses. Four thicknesses of LFP electrodes (including 20 μm thick Al foil), 80 μm, 150 μm, 190 μm, and 280 μm were prepared, corresponding to areal mass loadings of 14, 30, 40, and 60 mg cm⁻², respectively. Specifically, 6–60 μm through-hole arrays were successfully created in the electrodes with thicknesses of 80 μm, 150 μm, 190 μm (Fig. 4a–c and Supplementary Fig. 6), with a material loss ratio of less than 1%. However, this technique failed to fabricate through-holes in the 280 μm-thick LFP electrode (Fig. 4d), indicating the method has reached depth limit³⁷. The limit is mainly due to the high density of free electrons in the plasma plume, which causes significant reflection of the energy from subsequent pulses. When the beam is fully reflected and attenuated, the growth of the hole depth slows down and eventually stops³⁸.

In order to address this challenge, birefringent crystals of varying thickness were used to shape the ultraviolet laser temporally into multiple sub-pulses with different time delays. The experimental results demonstrated that through-holes (280 μm) were fabricated by temporal shaped femtosecond laser across all the pulse delays with 0.45 ps, 1.78 ps, 14.24 ps (Supplementary Fig. 7). However, the diameter of the through-hole increased when the pulse delay was 14.24 ps, a phenomenon also observed for the 190 μm thick LFP electrode (Supplementary Fig. 8). Eventually, the 0.45 ps sub-pulse delay was determined to be the best at drilling 6 μm through-holes in 280 μm-thick LFP electrodes, achieving an aspect ratio of 47 (Fig. 4e and Supplementary Fig. 9). This depth-to-diameter ratio is the highest known among opaque materials (Supplementary Table 3).

This high depth-to-diameter ratio is achieved through meticulous light modulation. When the energy surpasses the ablation threshold, it causes instant melting, vaporization, and ionization of the material³⁹. The debris generated during the fabrication of through-holes can be effectively removed using debris extraction systems such as smoke purifiers⁴⁰. The formation of through-holes is facilitated by multiple

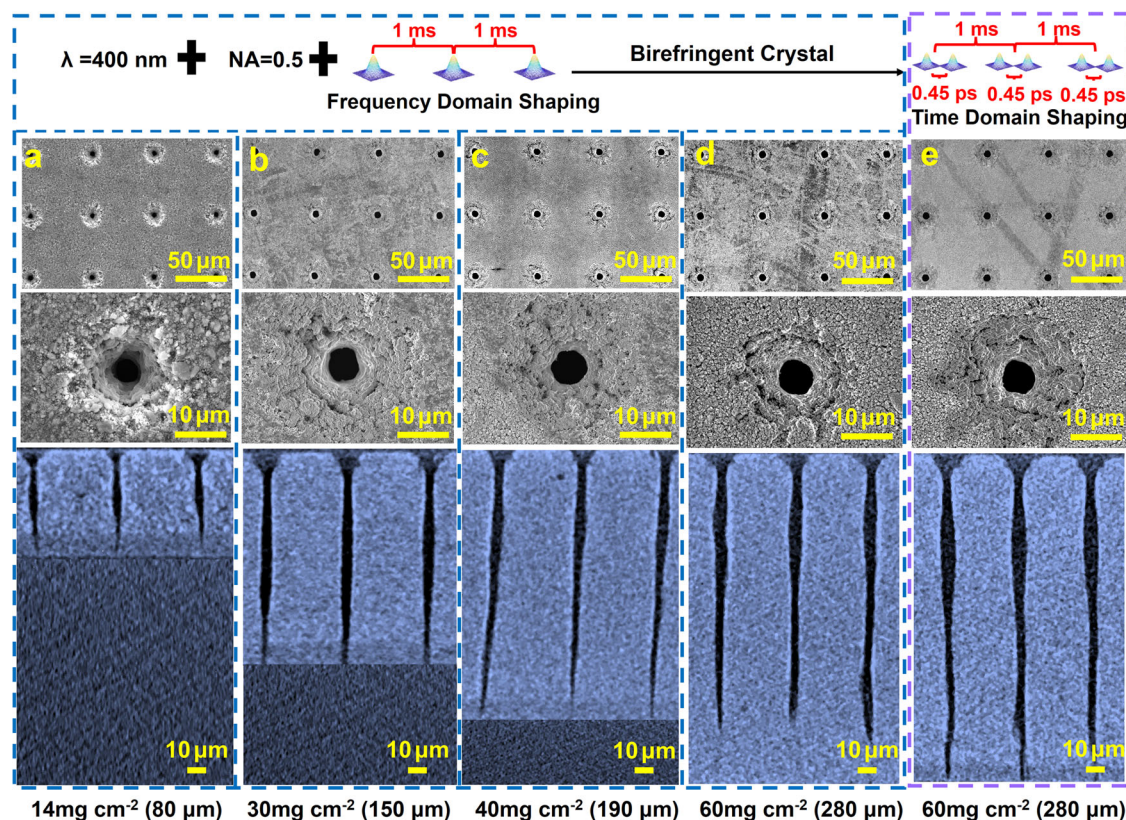


Fig. 4 | Through-hole arrays with 6–60 μm configuration in LFP electrodes with different areal mass loadings. SEM and X-ray tomography images of through-holes fabricated by frequency domain shaping on different thick electrodes: **a** 14 mg cm^{-2} (80 μm); **b** 30 mg cm^{-2} (150 μm); **c** 40 mg cm^{-2} (190 μm); **d** 60 mg cm^{-2} (280 μm). Through-holes fabricated by frequency and time domain shaping: **e** 60 mg cm^{-2} (280 μm).

electrodes does not impede ion diffusion until higher rates. At a mass loading of 30 mg cm^{-2} (Fig. 5b), there was an obvious capacity difference starting from 1 C. Specific capacities of 128, 97, and 41 mAh g^{-1} were achieved for laser-structured LFP at 1 C, 2 C, and 3 C, respectively, greatly exceeding the unstructured LFP, which delivered capacities of 113, 50, and 15 mAh g^{-1} at the same rates. At a mass loading of 40 mg cm^{-2} (Fig. 5c), the difference becomes evident at 0.5 C, indicating that high tortuosity becomes a major bottleneck for thick electrodes. At rates of 1 C, 1.5 C, and 2 C, the discharge capacities of laser-structured LFP were 130, 113, and 78 mAh g^{-1} , respectively, while unstructured LFP showed much lower capacities of 51, 20, and 9 mAh g^{-1} due to insufficient Li^+ supply through the highly tortuous structures at fast charging/discharging conditions. Even with a mass loading of 60 mg cm^{-2} (Fig. 5d), the laser-structured LFP maintained a capacity of 85 mAh g^{-1} at 1.5 C, whereas the unstructured LFP managed only 8 mAh g^{-1} . Generally, laser-drilled low-tortuosity structure can increase the power density of thick electrodes ($\geq 130 \mu\text{m}$) by 100–200% without compromising specific capacity.

Semiempirical models to extract the time constant (τ_{fit}) associated with the rate-limiting kinetic process were further applied to explain the rate enhancement, using the following equation⁴³:

$$\frac{C}{C_n} = 1 - \exp\left[\left(-\frac{t}{\tau_{fit}}\right)^\beta\right] \quad (3)$$

where C/C_n represents the normalized capacity, t is the discharge time, and τ_{fit} denotes the time constant of rate limiting process. A smaller τ_{fit} indicates faster ion transport, enabling Li^+ ions to access active sites more rapidly. As shown in the fitted curves (Supplementary Fig. 14) and summarized in Supplementary Table 4, electrodes with through-holes

exhibit significantly smaller τ_{fit} . This confirms that the through-hole architecture shortens ion transport pathways within thick electrodes, enhances ionic accessibility to active materials, and improves rate performance.

The significant improvement in power density allows for the use of thicker electrodes, thereby achieving higher areal capacity and enhancing energy density (Fig. 5h). However, accurately quantifying this increase in energy density is challenging, as energy density fluctuates with power density (Supplementary Fig. 15). A key requirement for using electrodes of specific thicknesses is maintaining good capacity retention at the desired operating rate. To this end, we established a baseline of at least 50% capacity retention (75 mAh g^{-1}) at the highest operating rate as the prerequisite for using electrodes of a certain thickness, and then we calculated the energy density increase based on the maximum energy density that the thickness can provide. As illustrated in Fig. 5f, if a 1 C rate is essential for the product, the increase in specific energy density from expanding the active material thickness from 156 μm (36 mg cm^{-2}) to 260 μm (60 mg cm^{-2}) would result in a specific energy density increase of 9.39%, according to Fig. 1d. Similarly, at rates of 1.5 C and 2 C, the specific energy density increase is determined to be 12.27% and 17.39%, respectively. Using the same criteria, we calculated that the increases in volumetric energy density are 14.92%, 19.48%, and 26.72% for 1 C, 1.5 C, and 2 C, respectively (Supplementary Fig. 15).

The observed improvement is attributed to the reduction in tortuosity. To quantify the tortuosity change, electrochemical impedance spectroscopy (EIS) of LFP || LFP symmetric cells was performed. The resulting impedance spectra were analyzed using the transmission-line model (TLM), which enables extraction of ionic resistance within the electrolyte phase of the porous positive electrode. Given the uniform and low-volume through-hole structure, the electrode can still be

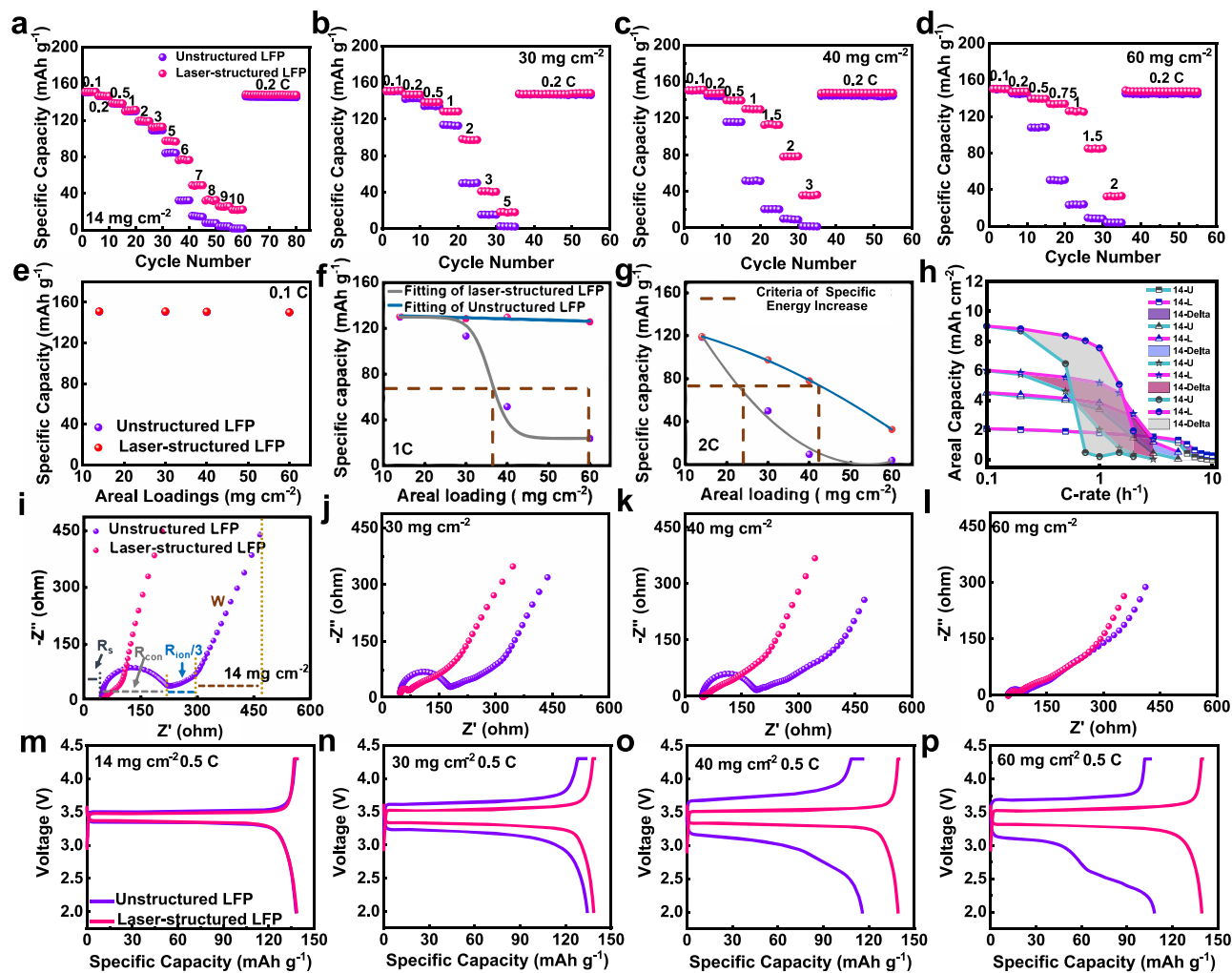


Fig. 5 | Electrochemical measurements of unstructured and laser-structured LFP electrodes with different thicknesses. Rate performance of unstructured and laser-structured LFP electrodes ($1\text{C} = 160\text{ mA g}^{-1}$) with different areal mass loadings of **a** 14 mg cm^{-2} , **b** 30 mg cm^{-2} , **c** 40 mg cm^{-2} , and **d** 60 mg cm^{-2} at various current densities. Capacity comparison curves of batteries at different charging and discharging rates: **e** 0.1C ; **f** 1C ; **g** 2C . **h** Areal discharge capacity for electrodes of

varying thickness. ‘Delta’ refers to the increase in areal discharge capacity at the same areal mass loading. **i–l** Electrochemical Impedance Spectroscopy (EIS) to measure the tortuosity of LFP electrodes in symmetric batteries. (The equivalent circuits are in Supplementary Fig. 22). **m–p** Charge-discharge voltage profiles of different LFP electrodes at 0.5C for **m** 14 mg cm^{-2} , **n** 30 mg cm^{-2} , **o** 40 mg cm^{-2} , and **p** 60 mg cm^{-2} .

considered homogeneous (Supplementary Note 2). The impedance response (Fig. 5i–l) can be deconvoluted into three components: (1) The resistance R_s , which accounts for the resistance of the electrolyte//separator, electric contact resistance, etc.; (2) A semicircle in the high-to-mid frequency, attributed to the electrode//current collector contact resistance (R_{con}); (3) Ionic resistance ($R_{ion}/3$) within the porous electrode, appearing in the low-to-mid frequency, which reflects ion transport resistance through electrolyte-filled pores within electrode structures. The tortuosity can be calculated using the following equation^{44,45}:

$$\tau = \frac{R_{ion} A \kappa \epsilon}{2d} \quad (4)$$

where τ is the tortuosity, R_{ion} is the ionic impedance, A is the cross-sectional area of the electrode, κ is the conductivity of the electrolyte, ϵ is the porosity, and d is the thickness of the electrode coating. A 10 mM solution of TBAClO_4 in EC/DEC ($w/w = 1:1$), with an ionic conductivity of $4.6 \times 10^{-4}\text{ S cm}^{-1}$, was used to meet the requirement for TLM ($R_{el}/R_{ion} < 10^{-2}$)⁴⁶. The EIS plots of unstructured LFP symmetric cells under different pressures demonstrate that the extracted ionic resistance

R_{ion} , and thus tortuosity, can be considered independent of R_{con} and R_s (Supplementary Fig. 16). The validity was confirmed by the invariance of ($R_{ion} \times \kappa$) across electrolytes with different conductivities (Supplementary Note 3, Supplementary Fig. 17). The ionic resistance and calculated tortuosity are shown in Table 1.

For electrodes with mass loadings of 14 , 30 , 40 , and 60 mg cm^{-2} , the measured tortuosity values were 2.62 , 2.57 , 2.58 , and 2.47 , respectively, indicating that tortuosity is largely independent of thickness in unstructured electrodes. After laser structuring, the tortuosity was consistently reduced to 2.02 , 2.08 , 2.09 , and 1.97 , respectively. These results demonstrate a robust and reproducible $\sim 20\%$ decrease in tortuosity across all electrode thicknesses, confirming the effectiveness of the through-hole architecture in shortening ionic transport path.

Galvanostatic intermittent titration technique (GITT) on both laser-structured and unstructured LFP electrodes was further performed to assess lithium-ion diffusion. GITT results revealed a notably lower IR overpotential in laser-structured electrodes, indicating reduced ionic resistance due to the through-hole array (Supplementary Fig. 18). Moreover, the potential can be reasonably approximated to exhibit a linear relationship with the concentration,

Table 1 | Comparison of the tortuosity of different electrodes

Areal mass loading (mg cm ⁻²)	Thickness of active materials (μm)	Ionic impedance R_{ion} (Ω) of unstructured LFP	Ionic impedance R_{ion} (Ω) laser-structured LFP	Tortuosity of unstructured LFP	Tortuosity of laser-structured LFP	Reduction of tortuosity
14	60	201.51	152.02	2.62	2.02	22.9%
30	130	428.20	338.17	2.57	2.08	19.1%
40	170	562.65	444.46	2.58	2.09	19.0%
60	260	641.86	823.26	2.47	1.97	20.2%

satisfying the requirement for validating the diffusion coefficient calculation (Supplementary Fig. 19). The Li⁺ diffusivity can be calculated using the classic Fickian model:

$$D = \frac{4L^2}{\pi\tau} \left(\frac{\Delta E_s}{\Delta E_t} \right)^2 \quad (5)$$

where D is the lithium-ion diffusion coefficient, L is the thickness of the active material layer, ΔE_t is the total voltage change during the current pulse, and ΔE_s is the steady-state voltage change after relaxation. Results (Supplementary Table 5) show significantly higher Li⁺ diffusivity in laser-structured electrodes. Although GITT aims to measure particle-level ion diffusivity, real electrode responses are also affected by tortuosity and electrolyte access. Unstructured LFP with high tortuosity delays equilibration, lowering $\Delta E_s/\Delta E_t$ and underestimating D . So laser-structured electrodes reduce these limitations, enabling faster ion redistribution, more accurate $\Delta E_s/\Delta E_t$, and thus a higher, more reliable diffusion coefficient, reflecting the architectural improvements.

Low-tortuosity structures reduce internal resistance and overpotential, thereby minimizing heat generation and energy loss, effects that become increasingly pronounced with thicker active material layers and higher charge/discharge rates (Fig. 5m-p and Supplementary Fig. 20). For electrodes with thicknesses of 190 μm and 280 μm operating at 0.5 C, the energy efficiencies of the laser-structured electrodes have significantly increased from ~76% (unstructured LFP electrode) to 92%, representing a substantial energy saving (Supplementary Table 6). The energy loss, usually wasted as heat, presents a significant risk for fast charging and discharging. This was further confirmed by cyclic voltammetry (CV) results (Supplementary Fig. 21). At a scan rate of 0.05 mV s⁻¹, the discharge and charge peaks were respectively observed at 3.2 V and 3.6 V, corresponding to the two-phase transition between FePO₄ and LiFePO₄⁴⁷. The laser-structured electrode exhibits sharper redox peaks and much lower overpotential than the unstructured electrode, indicating faster ion diffusion and smaller overpotentials. Therefore, the low-tortuosity structure is advantageous for high-power operations.

The laser-structured LFP electrode also demonstrated enhanced cycling performance compared to its unstructured counterpart. Both structured and unstructured LFP electrodes were paired with lithium metal for cycling tests (Fig. 6a-c). At a rate of 0.2 C, all the batteries with unstructured thick electrodes, regardless of the thickness, could only sustain 40–60 cycles, whereas those with laser-structured electrodes reached 150 cycles, marking an enhancement in cycling lifetime. The same trend was also observed for 0.5 C (Fig. 6d-f).

The laser structuring technique has done low damage to active materials, as verified by high temperature tests. Both laser-structured and unstructured LFP half-cells were fully charged and stored at 60 °C for over 200 h to assess self-discharge (Supplementary Fig. 23a). The similar voltage retention profiles indicate that laser processing does not introduce reactive surface, suggesting no additional side reactions. Galvanostatic cycling at 60 °C (Supplementary Fig. 23b-c) showed that laser-structured electrodes exceeded unstructured ones across

different thicknesses (14 and 40 mg cm⁻²), demonstrating the same improved cycle stability at elevated temperature.

The laser shaping method has a wide material applicability, since laser can process any material. 6–60 μm through-hole arrays were further fabricated in NMC electrodes (Fig. 7a-b and Supplementary Fig. 24) with two thicknesses (60 μm, 160 μm) corresponding to areal mass loadings of 14, 50 mg cm⁻², respectively. For the 60 μm thick NMC electrode, the laser-structured NMC electrode demonstrated capacities of 156 mAh g⁻¹ at 1 C and 113 mAh g⁻¹ at 5 C. This is an improvement over the unstructured NMC electrode (Supplementary Fig. 25), which delivers only 127 mAh g⁻¹ at 1 C and 4 mAh g⁻¹ at 5 C (Fig. 7c), roughly 5 times improvement in rate performance. For the 160 μm thick NMC electrode, the laser-structured NMC electrode exhibited a roughly 100% improvement in rate performance, delivering a specific capacity of 93 mAh g⁻¹ at 1.5 C (Fig. 7d), while the unstructured electrode can only operate at 0.75 C to show similar capacity. Similarly, the introduction of through-holes in the NMC electrode effectively reduces its overpotential (Supplementary Fig. 26).

The negative electrode is another critical limiting factor in fast charging. Graphite particles are typically large (>10 μm), increasing tortuosity and restricting Li⁺ diffusion. This inadequate ion transport can lead to inhomogeneous lithiation and even metallic lithium plating, not only reducing capacity but also posing safety risks⁴⁸. Laser structuring alleviates these limitations by enabling more uniform and faster Li⁺ transport throughout the electrode. Although the size of graphite particles often exceeds the hole size, our experiments demonstrate that high-energy femtosecond laser pulses can effectively fabricate 6–60 μm through-hole array in graphite negative electrodes, irrespective of particle size (Supplementary Fig. 27). This highlights the versatility and efficacy of our approach for both electrode positive and negative electrode applications, ultimately enhancing rate capability and improving long-term cycling performance.

Discussion

This study successfully demonstrated a frequency and time-domain laser shaping technique to fabricate low-tortuosity LFP and NMC thick electrodes with low material loss. By manufacturing micropore arrays in the electrodes via femtosecond laser drilling, we successfully enhanced the energy density, power density, and cycling lifetime of batteries, presenting a promising avenue for the development of high-performance, durable, and fast charging/discharging lithium-ion batteries.

Currently, our approach utilizes laser direct writing, a method that is inherently slow, with a fabrication rate of 3–5 holes per second. To enable large-scale industrial applications, manufacturing speed needs to be improved. One promising strategy is beam splitting, which was demonstrated here using a diffractive optical element (DOE) to divide the laser beam into a 1 × 4 array, increasing the processing speed by fourfold, achieving 12–20 holes per second (Supplementary Figs. 28–29). For industrial-scale production, the use of high-repetition-rate lasers (in the MHz range) in combination with customized DOE beam splitters can enable far greater parallelization. For instance, a 100 × 100 beam array could theoretically deliver over 10,000 simultaneous beamlets, enabling processing speeds of

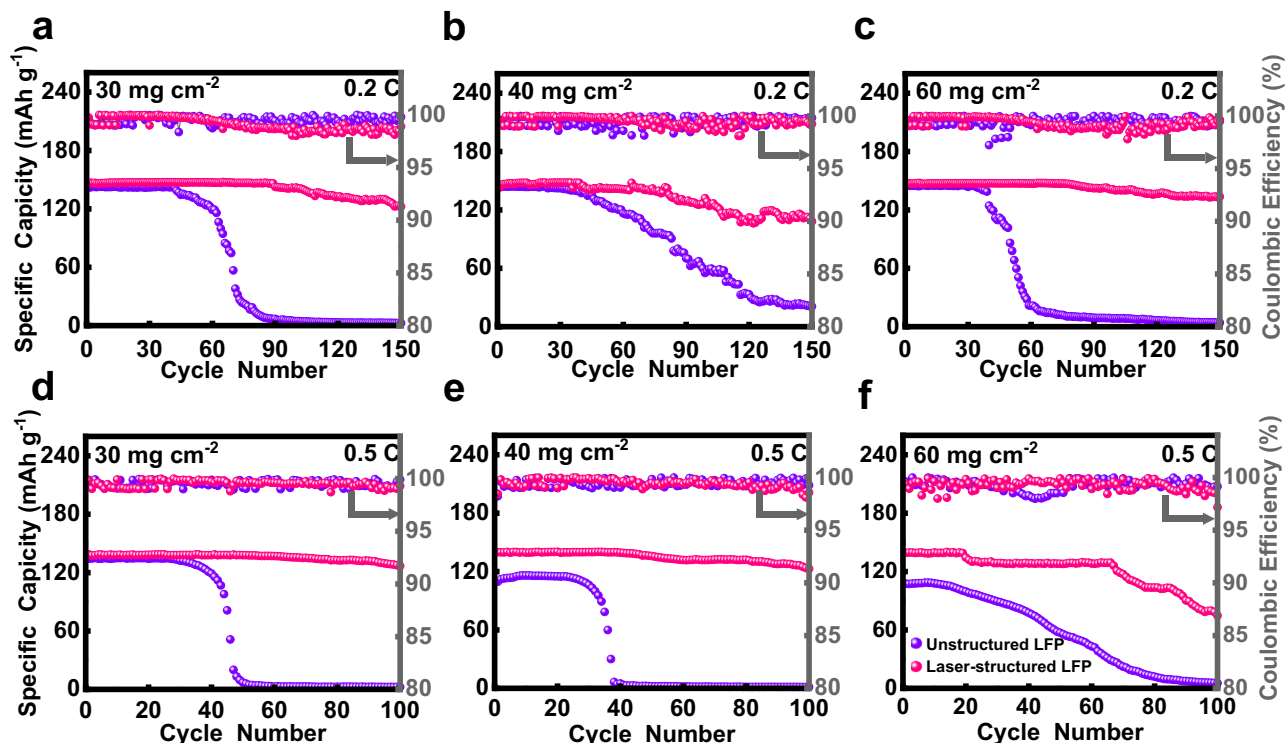


Fig. 6 | Comparison of cycling stability (1 C = 160 mA g⁻¹, Li||LFP) of unstructured and laser-structured LFP electrodes with different thicknesses. The comparison of cycling performance at 0.2 C for **a** 30 mg cm⁻², **b** 40 mg cm⁻², and

c 60 mg cm⁻². The comparison of cycling performance at 0.5 C for **d** 30 mg cm⁻², **e** 40 mg cm⁻², and **f** 60 mg cm⁻².

30,000–50,000 holes per second, as already demonstrated in through glass via (TGV) by using a femtosecond Bessel beam⁴⁹. Then the processing rate of 6–60 μm structure would be 1 cm² s⁻¹, satisfying the typical industrial takt time requirement. By integrating laser beam splitting and debris extraction systems, the proposed technique is compatible with calendared electrodes and roll-to-roll production, enabling scalable processing for industrial-scale manufacturing lines (Supplementary Fig. 30). Future research will explore more high-speed laser drilling methods and evaluate how microstructural modifications influence battery performance under real-world operating conditions.

Methods

Laser percussion drilling on thick electrodes

The femtosecond pulsed laser system (Spectra physics; Ti:sapphire, 35 fs, 800 nm, 1 kHz) provided the ultra-short 800 nm laser pulses (Fig. 1f). The laser beam was directed through a BBO crystal (BaB₂O₄, Fuzhou Yujing Optoelectronic Technology Co., Ltd.) and an optical filter to double the frequency of the 800 nm laser light, converting it to 400 nm. Then a birefringent crystal (Chenjing Optoelectronics Co., Ltd) was used to temporally shape the Gaussian pulses into double-pulse trains (subpulse energy ratio, 1:1) with crystal thicknesses and corresponding time delays of 0.8 mm–0.45 ps; 3.2 mm–1.78 ps; 25.6 mm–14.24 ps, respectively. A mechanical shutter was applied to obtain the desired number of pulses. A charge-coupled device (CCD) camera was used to visualize the sample surface and to position it at the beam focus. The temporally shaped ultraviolet pulses were reflected by a dichroic mirror and then focused by a long-focus 50 \times objective lens (NA = 0.5, Olympus) onto the electrode, installed on an xyz translation stage driven by a computer-controlled system. After the diaphragm was adjusted to limit the laser beam to a spot diameter of 2 mm, we tested the laser energy. Laser percussion drilling used 300 shots ($t = 0.3$ s) with a pulse energy of 35 μJ (Fig. 2a-d). The single pulse energies used for drilling LFP electrode with thicknesses of

80 μm , 150 μm , 190 μm , and 280 μm are 10 μJ , 20 μJ , 30 μJ , and 60 μJ , respectively (Fig. 4a-d). The single pulse energies used for drilling the NMC electrodes with thicknesses of 60 μm , 160 μm are respectively 10 μJ , 20 μJ (Fig. 7a-b). All electrodes were commercially sourced from Hefei Frontier New Material Co., Ltd., and produced via the tape-casting method. For the electrode composition, both NMC and LFP electrodes consisted of polyvinylidene fluoride (PVDF) as the binder, conductive carbon black, carbon nanotube, and either LFP or NMC as the active material, with respective weight ratios of 1.5%, 2%, 0.5%, and 96%. The particle sizes (D50) of LFP and NMC were ~0.6–1.8 μm and 10 μm , respectively, measured by a Malvern MS-2000 laser particle size analyzer. The detailed particle size distributions are provided in Supplementary Table 7.

Characterization

The surface morphology of the low-tortuosity thick electrodes was obtained by on a field emission scanning electron microscope (SEM, Regulus 8230, Hitachi) working at 5 kV. The elemental composition analysis was conducted via an X-ray spectrometer (EDS, Bruker) operated at 6 kV. For the three-dimensional reconstruction of internal morphology, a high-resolution X-ray tomography with ZEISS reconstruction (XRT, Xradia 520 Versa, ZEISS) with was used, with the beam energy set to 60 kV and the beam current set to 93 μA for imaging. The morphology of the upper and lower surface through-holes was obtained by an optical microscope BX 51 (Olympus), in which both the electrode material and the current collector were penetrated.

Electrochemical testing

Coin-type half-cells using the CR2032 (304 stainless steel, Kelude Co., Ltd.) casing format were assembled in an Ar-filled glovebox using Li foils (thickness of 1 mm, diameter of 16 mm) as counter electrodes, polypropylene film (Celgard 2500, diameter of 19 mm) as separators, single-side coated LFP/NMC 811 electrodes (square, 5 \times 5 mm), and

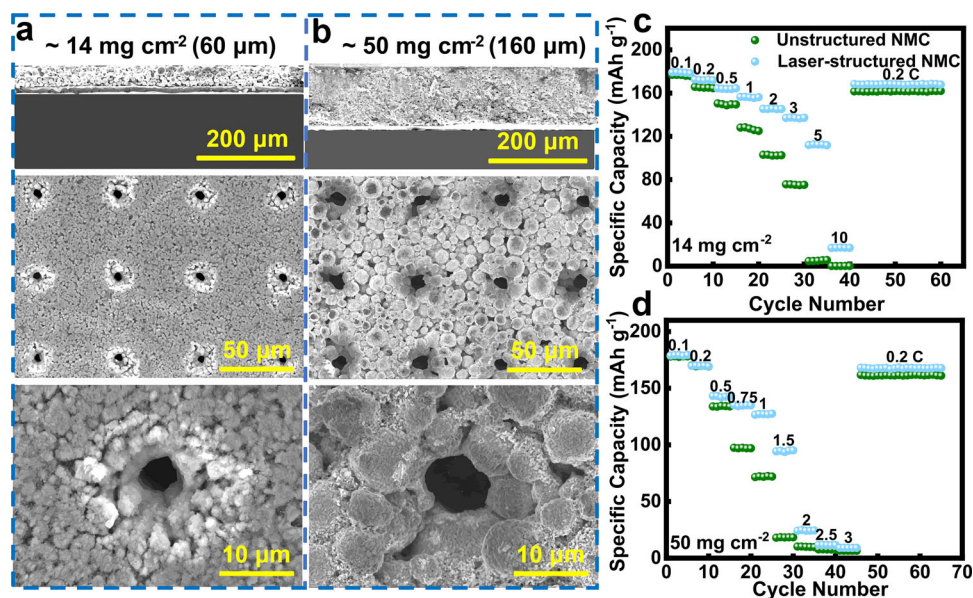


Fig. 7 | Surface morphology of the through-hole array and electrochemical performance of $\text{LiNi}_0.5\text{Co}_0.3\text{Mn}_{1.0}\text{O}_2$ (NMC) electrodes. a, b Scanning Electron Microscope (SEM) images of the laser-structured 6–60 μm NMC electrode.

c, d Rate performance (1 C = 180 mA g^{-1}) of unstructured and laser-structured NMC electrodes with different areal mass loadings of **c** 14 mg cm^{-2} , and **d** 50 mg cm^{-2} .

30 μL of electrolyte—1.0 M LiPF_6 dissolved in a mixture of ethylene carbonate (EC): diethyl carbonate (DEC) with a volume ratio of 1:1 (Dodochem Co., Ltd.). All battery charge-discharge tests and GITT measurements, with data recorded at a frequency of 1 data point per 10 seconds, were conducted on a LAND-CT3002A battery test instrument (Lanhe, RS422 Protocol, Wuhan). LFP/NMC batteries were tested in the voltage range of -2.0–4.3 V / -2.5–4.3 V under constant current/constant voltage charge. And a 1 C rate corresponds to a specific current of 160 mA g^{-1} for LFP, and a specific current of 180 mA g^{-1} for NMC. Two cycles of charge-discharge at 0.1 C were performed before the battery performance testing phase. And the cutoff capacity for the LFP half-cell is 160 mAh g^{-1} , and that for the NMC half-cell is 180 mAh g^{-1} . CV measurements were taken at a scan rate of 0.05 mV s^{-1} and in the range of 2.8–4.3 V. The tortuosity tests were performed using pouch cells with EIS tests. AC impedance measurements were taken in the frequency range of 0.01 Hz– 10^5 Hz at open circuit potential with a 5 mV amplitude. During tortuosity measurements, the electrode is circular with a diameter of 12 mm without charging; the electrolyte used is 10 mM TBAClO_4 (98%, Macklin) in EC/DEC w/w = 1:1 with a conductivity of 0.46 mS cm^{-1} ; and ϵ is 30% for unstructured electrodes and 30.7% for laser structured electrode. These tests were carried out on a CHI 760E electrochemistry workstation from Shanghai Chenhua Instrument, Inc. All electrochemical tests were conducted at temperature of 26 ± 3 °C. For each single electrochemical experiment, three cells were tested to ensure the reliability of the data.

Electrochemical simulation

Electrochemical modeling and simulation of unstructured LFP and laser-structured LFP electrodes with different configurations were carried out using COMSOL Multiphysics 5.4. Given the favorable heat dissipation conditions, the half-cell models during battery operation were considered to be isothermal. Since the nanoparticles and pores within the LFP porous electrodes were much smaller compared to the overall electrodes, these electrodes were simplified as a homogeneous medium. The diffusion of lithium in LFP particles was depicted using Fick's laws, while ion transport in the electrolyte was modeled via the concentrated solution theory⁵⁰. The charge transfer rate at the electrode-electrolyte interfaces was governed by the Butler-Volmer kinetics. The detailed model parameters are presented in Supplementary Table 8.

Beam splitting

A laser beam splitter suitable for 800 nm femtosecond lasers (MS-629-800-Y-A, $\theta_f = 2.26$, Holoor) was customized, which can reshape the original Gaussian-shaped femtosecond laser into a 1×4 laser beam array. Except for the differences in power and propagation direction, other parameters of the reshaped laser, such as repetition frequency (1 kHz) and pulse width (35 fs), are the same as those of the femtosecond laser before reshaping. Specifically, the beam splitter was placed in front of a 20× short focal length objective lens (NA = 0.45, Olympus) and the pulse delay of temporally shaped femtosecond laser is 0.45 ps. The single pulse energy used for high-efficiency drilling on the LFP electrodes (14 mg cm^{-2}) is 50 μJ (Supplementary Figs. 27–28).

Data availability

The authors declare that the data supporting the findings of this study are available within this article and its Supplementary Information, or from the corresponding authors upon request. Source data are provided with this paper.

References

- Jain, R. et al. Nanostructuring versus microstructuring in battery electrodes. *Nat. Rev. Mater.* **7**, 736–746 (2022).
- Li, S. et al. Progress and perspective of ceramic/polymer composite solid electrolytes for lithium batteries. *Adv. Sci.* **7**, 5 (2020).
- Wang, C., Yang, C. & Zheng, Z. Toward practical high-energy and high-power lithium battery anodes: present and future. *Adv. Sci.* **9**, 9 (2022).
- Zhao, S. et al. Towards high-energy-density lithium-ion batteries: Strategies for developing high-capacity lithium-rich cathode materials. *Energy Storage Mater.* **34**, 716–734 (2021).
- Chen, H. et al. Free-standing ultrathin lithium metal-graphene oxide host foils with controllable thickness for lithium batteries. *Nat. Energy* **6**, 790–798 (2021).
- Kittner, N., Lill, F. & Kammen, D. M. Energy storage deployment and innovation for the clean energy transition. *Nat. Energy* **2**, 17125 (2017).
- Randau, S. et al. Benchmarking the performance of all-solid-state lithium batteries. *Nat. Energy* **5**, 259–270 (2020).

8. Yang, C., Fu, K., Zhang, Y., Hitz, E. & Hu, L. Protected lithium-metal anodes in batteries: from liquid to solid. *Adv. Mater.* **29**, 36 (2017).
9. Kuang, Y., Chen, C., Kirsch, D. & Hu, L. Thick electrode batteries: principles, opportunities, and challenges. *Adv. Energy Mater.* **9**, 1901457 (2019).
10. Shi, B. et al. Low tortuous, highly conductive, and high-area-capacity battery electrodes enabled by through-thickness aligned carbon fiber framework. *Nano Lett.* **20**, 5504–5512 (2020).
11. Wang, Y., Fu, X., Zheng, M., Zhong, W. H. & Cao, G. Strategies for building robust traffic networks in advanced energy storage devices: a focus on composite electrodes. *Adv. Mater.* **31**, 1804204 (2018).
12. Boyce, A. M. et al. Design of scalable, next-generation thick electrodes: opportunities and challenges. *ACS Nano* **15**, 18624–18632 (2021).
13. Li, H. et al. Ultrahigh-capacity and fire-resistant LiFePO₄-based composite cathodes for advanced lithium-ion batteries. *Adv. Energy Mater.* **9**, 1802930 (2019).
14. Liu, W. et al. Designing polymer-in-salt electrolyte and fully infiltrated 3D electrode for integrated solid-state lithium batteries. *Angew. Chem. Int. Ed.* **60**, 12931–12940 (2021).
15. Xia, Y. et al. Thickness-independent capacitance of vertically aligned liquid-crystalline MXenes. *Nature* **557**, 409–412 (2018).
16. Sun, H. et al. Hierarchical 3D electrodes for electrochemical energy storage. *Nat. Rev. Mater.* **4**, 45–60 (2018).
17. Arnot, D. J. et al. Thick electrode design for facile electron and ion transport: architectures, advanced characterization, and modeling. *Acc. Mater. Res.* **3**, 472–483 (2022).
18. Zhao, Z. et al. Sandwich, vertical-channeled thick electrodes with high rate and cycle performance. *Adv. Funct. Mater.* **29**, 1809196 (2019).
19. Li, L., Erb, R. M., Wang, J., Wang, J. & Chiang, Y. M. Fabrication of low-tortuosity ultrahigh-area-capacity battery electrodes through magnetic alignment of emulsion-based slurries. *Adv. Energy Mater.* **9**, 1802472 (2018).
20. Wu, J. et al. Ultrahigh-capacity and scalable architected battery electrodes via tortuosity modulation. *ACS Nano* **15**, 19109–19118 (2021).
21. Delattre, B. et al. Impact of pore tortuosity on electrode kinetics in lithium battery electrodes: study in directionally freeze-cast LiNi_{0.8}Co_{0.15}Al_{0.05}O₂(NCA). *J. Electrochem. Soc.* **165**, A388–A395 (2018).
22. Dang, D., Wang, Y., Gao, S. & Cheng, Y.-T. Freeze-dried low-tortuous graphite electrodes with enhanced capacity utilization and rate capability. *Carbon* **159**, 133–139 (2020).
23. Zhang, X. et al. Tunable porous electrode architectures for enhanced Li-ion storage kinetics in thick electrodes. *Nano Lett.* **21**, 5896–5904 (2021).
24. Abdollahifar, M. et al. Insights into influencing electrode calendaring on the battery performance. *Adv. Energy Mater.* **13**, 2300973 (2023).
25. Zhang, J., Huang, H. & Sun, J. Investigation on mechanical and microstructural evolution of lithium-ion battery electrode during the calendaring process. *Powder Technol.* **409**, 117828 (2022).
26. Smyrek, P., Pröll, J., Seifert, H. J. & Pfleging, W. Laser-induced breakdown spectroscopy of laser-structured Li(NiMnCo)O₂ Electrodes for Lithium-Ion Batteries. *J. Electrochem. Soc.* **163**, A19–A26 (2015).
27. Kohler, R. et al. Laser micro-structuring of magnetron-sputtered SnO_x thin films as anode material for lithium ion batteries. *Microsyst. Technol.* **17**, 225–232 (2011).
28. Wu, J. et al. Controllable photoexfoliation of monolayer graphene quantum dots using temporally and spatially shaped femtosecond laser. *Carbon* **230**, 119667 (2024).
29. Jia, X., Chen, Y., Liu, L., Wang, C. & Duan, J. Advances in laser drilling of structural ceramics. *Nanomaterials* **12**, 230 (2022).
30. Lu, Y. M., Duan, Y. Z., Liu, X. Q., Chen, Q. D. & Sun, H. B. High-quality rapid laser drilling of transparent hard materials. *ACS Sustain. Chem. Eng.* **47**, 921–924 (2022).
31. Sun, X. et al. Ultrafast laser drilling of 3D porous current collectors for high-capacity electrodes of rechargeable batteries. *ACS Sustain. Chem. Eng.* **11**, 7357–7366 (2023).
32. Emani, H., et al. Laser Patterned Flexible Cathode with Low Tortuosity for Fast Charging Lithium-Ion Battery Applications. In: *2023 IEEE International Conference on Flexible and Printable Sensors and Systems (FLEPS)*. (IEEE, 2023).
33. Chen, K.-H. et al. Efficient fast-charging of lithium-ion batteries enabled by laser-patterned three-dimensional graphite anode architectures. *J. Power Sources* **471**, 228475 (2020).
34. Meyer, A., Ball, F. & Pfleging, W. High repetition ultrafast laser ablation of graphite and silicon/graphite composite electrodes for lithium-ion batteries. *J. Laser Appl.* **35**, 4 (2023).
35. Li, F. et al. Research on Microhole Processing Technology Based on the Femtosecond-Laser Spiral Trepanning Method. *Adv. Sci.* **10**, 7508 (2020).
36. Ferrer, A., Diez-Blanco, V., Ruiz, A., Siegel, J. & Solis, J. Deep sub-surface optical waveguides produced by direct writing with femtosecond laser pulses in fused silica and phosphate glass. *Appl. Surf. Sci.* **254**, 1121–1125 (2007).
37. Xia, B., Jiang, L., Li, X., Yan, X. & Lu, Y. Mechanism and elimination of bending effect in femtosecond laser deep-hole drilling. *Opt. Express* **23**, 27853–27864 (2015).
38. Panchenko, A. N. et al. Pulsed IR laser ablation of organic polymers in air: shielding effects and plasma pipe formation. *J. Phys. D Appl. Phys.* **44**, 385201 (2011).
39. Breittling, D., et al. Fundamental aspects in machining of metals with short and ultrashort laser pulses. In: *Photon Processing in Micro-electronics and Photonics III* (2004).
40. Wang, Q., Zhang, R., Chen, Q. & Duan, R. A review of femtosecond laser processing of silicon carbide. *Micromachines* **15**, 639 (2024).
41. Jiang, L. et al. Femtosecond laser high-efficiency drilling of high-aspect-ratio microholes based on free-electron-density adjustments. *Appl. Opt.* **53**, 98–101 (2014).
42. Wang, Z. et al. High-throughput microchannel fabrication in fused silica by temporally shaped femtosecond laser Bessel-beam-assisted chemical etching. *Opt. Lett.* **43**, 98–101 (2017).
43. Wu, J. et al. Low-tortuosity thick electrodes with active materials gradient design for enhanced energy storage. *ACS Nano* **16**, 4805–4812 (2022).
44. Landesfeind, J., Hattendorff, J., Ehrh, A., Wall, W. A. & Gasteiger, H. A. Tortuosity determination of battery electrodes and separators by impedance spectroscopy. *J. Electrochem. Soc.* **163**, A1373 (2016).
45. Guo, Y. et al. Determination of the tortuosity and contact resistances in thick graphite anodes via electrochemical impedance spectroscopy. *J. Power Sources* **569**, 233003 (2023).
46. Landesfeind, J., Ebner, M., Eldiven, A., Wood, V. & Gasteiger, H. A. Tortuosity of battery electrodes: validation of impedance-derived values and critical comparison with 3D tomography. *J. Electrochem. Soc.* **165**, A469–A476 (2018).
47. Huang, C., Dontigny, M., Zaghbi, K. & Grant, P. S. Low-tortuosity and graded lithium ion battery cathodes by ice templating. *J. Mater. Chem. A* **7**, 21421–21431 (2019).
48. Ho, A. S. et al. 3D detection of lithiation and lithium plating in graphite anodes during fast charging. *ACS Nano* **15**, 10480–10487 (2021).
49. Yao, Z. et al. High-efficiency fabrication of computer-generated holograms in silica glass using a femtosecond Bessel beam. *Opt. Laser Technol.* **135**, 106729 (2021).

50. Li, S. et al. Unveiling low-tortuous effect on electrochemical performance toward ultrathick LiFePO_4 electrode with 100 mg cm^{-2} area loading. *J. Power Sources* **515**, 230588 (2021).

Acknowledgements

This work is supported by the National Natural Science Foundation of China (Grant No. 22379012) and the Fundamental Research Funds for the Central Universities. Q. C. and J. R. W. also want to thank the funding support from Shenzhen Thinkpart Materials Technology Co., Ltd (Contract No. 202320341279 A). X. L. wants to thank the National Natural Science Foundation of China (Grant No. 52275401); L. J. wants to thank the National Natural Science Foundation of China (Grant No. 52235009) and the Chongqing Natural Science Foundation of China (Grant cstc2021jcyj-cxttX0003).

Author contributions

Q.C., X.L., and J.R.W. developed the methodology for this study. J.R.W. was responsible for the investigation and acquisition of experimental data. The manuscript was drafted and written by Q.C. and J.R. W.H.X.G., R.X.W., X.B.L., and Y.L. carried out the simulation work. J.Z., R.C.J., M.Y.T., X.F.W., and R.Z. analyzed the experimental results obtained in this research. Q.C., L.J., and X.L. supervised the overall study and secured the funding required for the project. All authors participated in the discussions regarding the research progress and results, and contributed to data analysis.

Competing interests

The authors declare no competing interests.

Additional information

Supplementary information The online version contains supplementary material available at <https://doi.org/10.1038/s41467-025-67702-8>.

Correspondence and requests for materials should be addressed to Xin Li or Qian Cheng.

Peer review information *Nature Communications* thanks the anonymous reviewer(s) for their contribution to the peer review of this work. A peer review file is available.

Reprints and permissions information is available at <http://www.nature.com/reprints>

Publisher's note Springer Nature remains neutral with regard to jurisdictional claims in published maps and institutional affiliations.

Open Access This article is licensed under a Creative Commons Attribution-NonCommercial-NoDerivatives 4.0 International License, which permits any non-commercial use, sharing, distribution and reproduction in any medium or format, as long as you give appropriate credit to the original author(s) and the source, provide a link to the Creative Commons licence, and indicate if you modified the licensed material. You do not have permission under this licence to share adapted material derived from this article or parts of it. The images or other third party material in this article are included in the article's Creative Commons licence, unless indicated otherwise in a credit line to the material. If material is not included in the article's Creative Commons licence and your intended use is not permitted by statutory regulation or exceeds the permitted use, you will need to obtain permission directly from the copyright holder. To view a copy of this licence, visit <http://creativecommons.org/licenses/by-nc-nd/4.0/>.

© The Author(s) 2025